minerals

MDPI

*Article*

# Recovery of Iron from a Refractory High-Alumina Hematite–Goethite Ore in Shanxi, China, by Suspension Reduction Roasting

**Kai Zou [1,2,3], Chao Chen [1,2,3,*], Yaohui Yang [1,2,3], Zhenya Zhou [1,2,3] and Wangni Wu [1,2,3]**

[1] Institute of Multipurpose Utilization of Mineral Resource, Chinese Academy of Geological Sciences, Chengdu 610041, China
[2] Research Center of Multipurpose Utilization of Metal Mineral Resources of China Geological Survey, Chengdu 610041, China
[3] Technology Innovation Center for Comprehensive Utilization of Strategic Mineral Resources, Ministry of Natural Resources, Chengdu 610041, China
* Correspondence: cagschenchao@163.com; Tel.: +86-18280101125

**Abstract**

The efficient recovery of iron from low-grade, high-alumina hematite–goethite ores is challenging because of their complex mineralogy and fine dissemination. This study investigates suspension reduction roasting followed by magnetic separation for a refractory ore from Shanxi, China. Under the preferred single-factor conditions identified within the tested ranges, magnetic separation yielded a concentrate with 56.67% Fe and an overall iron recovery of 87.83%. The key contribution is to show that selective conversion of iron minerals into magnetite can be achieved while maintaining distinct phase boundaries between Fe-rich and Al/Si-rich gangue, thereby limiting encapsulation of aluminosilicate minerals. Chemical phase analysis showed that the iron distribution in the magnetic fraction (magnetite plus pyrrhotite) increased from 0.08% in the raw ore to 92.07% after roasting. SEM–EDS showed that the newly formed Fe-rich phases remained spatially distinct from the gangue matrix. Mechanistically, thermodynamic analysis and phase characterization are consistent with a selective FeOOH → $Fe_2O_3$ → $Fe_3O_4$ pathway under the preferred conditions. Excessive reduction (overly high temperatures or reducing atmospheres) may have promoted FeO and fayalite formation and potentially degraded magnetic separation performance; however, these over-reduction products were not directly identified in this study.

**Keywords:** high-alumina hematite–goethite ore; suspension reduction roasting; magnetic separation; phase transformation; thermodynamic analysis

Check for updates

Academic Editor: Sunil K. Tripathy

Received: 21 August 2026
Revised: 10 November 2026
Accepted: 11 November 2026
Published: 16 November 2026

**Copyright:** © 2026 by the authors. Licensee MDPI, Basel, Switzerland. This article is an open access article distributed under the terms and conditions of the Creative Commons Attribution (CC BY) license.

## 1. Introduction

Iron ore is an essential raw material for the iron and steel industry, and its efficient utilization is crucial for the sustainable development of the steel industry [1]. With the continuous depletion of high-quality magnetite resources globally, the focus of iron ore processing has shifted to weakly magnetic hematite and goethite, which are difficult to process and smelt [2]. This challenge is particularly acute in China, where the average grade of domestic iron ore is only approximately 34.5% TFe, and external dependence on imported iron ore has remained above 80% for an extended period [3]. Consequently, there is an urgent economic and strategic imperative to develop efficient technologies for domestic low-grade iron ores. Among these, the high-alumina hematite–goethite ore from the sedimentary-weathered crust type Shanxi-type iron deposit in Jiaokou County is a highly

 https://doi.org/10.3390/min16111193

representative example. With an average grade of approximately 32% TFe, this ore is characterized by the fine dissemination of hematite and goethite within aluminosilicate gangue [4]. These ores are generally characterized by low iron grade, high alumina and silica contents, and complex mineral intergrowth relationships [5]. Specifically, the iron minerals are intimately intergrown with aluminum-bearing gangue minerals, including aluminosilicates (e.g., kaolinite) and aluminum oxyhydroxides (e.g., diaspore, AlO(OH)). This intimate intergrowth hinders the effective separation of iron minerals from gangue via conventional beneficiation processes, leading to low resource utilization [6–8]. Therefore, it is imperative to develop efficient and environmentally friendly processing technologies to unlock the utilization of these abundant but refractory high-alumina hematite–goethite ores.

Currently, the processing technologies for hematite–goethite resources mainly include magnetic separation, flotation, and magnetization roasting–magnetic separation combined processes [9,10]. Since both hematite and goethite are weakly magnetic minerals, direct magnetic separation cannot readily yield ideal separation indices [11–13]. While flotation is capable of effecting the selective separation of iron minerals from gangue, it is encumbered by significant reagent consumption, intricate process flowsheets, and a notable environmental burden [14–16]. Reductive roasting followed by magnetic separation has therefore been extensively studied as a technically viable alternative for such refractory ores. As summarized by Bulayani et al. [17], previous studies on reduction roasting followed by magnetic separation have employed various reductants (e.g., coal, cow dung, sodium bicarbonate, and $H_2$) under widely varying conditions (temperatures of 500–1050 °C and times of 20–80 min) to upgrade ores of different grades and particle sizes. Similarly, Xue et al. [5] demonstrated that the type and concentration of alumina-bearing minerals significantly influence the high-temperature processing characteristics of high-alumina iron ores. These studies establish the methodological foundation for reduction roasting-magnetic separation. However, traditional magnetization roasting using fixed beds or rotary kilns generally exhibits shortcomings such as long roasting time, high energy consumption, and low gas–solid heat and mass transfer efficiency [18,19].

In recent years, suspension reduction magnetization roasting technology has attracted extensive attention owing to its excellent gas–solid flow characteristics and highly efficient heat and mass transfer characteristics [20]. Compared with conventional roasting processes, suspension roasting can achieve rapid reduction and magnetization transformation of iron minerals in a relatively short time, which has the theoretical potential to reduce energy consumption and enhance processing efficiency compared to conventional methods [21–23]. Previous studies have shown that this technology has promising application prospects in the recovery of hematite, goethite, and iron tailings [24–26]. Nevertheless, previous research has mainly focused on the optimization of process parameters and the evaluation of separation performance, while studies on the thermodynamic transformation laws of iron minerals and the phase evolution mechanisms during magnetization roasting in high-alumina hematite–goethite systems remain relatively scarce [19,27].

Previous work by Jang et al. [28] investigated the chemical and mineral transformation of a low-grade goethite ore through dehydroxylation and reduction roasting, providing a direct prior-study comparator for thermal transformation and magnetic beneficiation; however, because different ores and roasting atmospheres cannot be assumed to behave identically, the specific response of complex, high-alumina refractory ores (like the Shanxi-type ore in this study) requires further quantification. While previous studies have investigated the reduction kinetics of iron oxides or the transformation of pure goethite [20,24,26,29], the behavior of high-alumina multicomponent systems remains less understood. Unlike studies focusing solely on magnetite growth kinetics [29], this work uniquely establishes the thermodynamic stability window and phase partitioning behavior for a multicomponent

system containing intimately intergrown aluminosilicates (kaolinite) and aluminum oxyhydroxides (diaspore). The primary contribution of this study is to elucidate the ore-specific alumina-related behavior that governs the selective reduction window and subsequent magnetic separation efficiency. In view of this, the present study investigates a high-alumina refractory hematite–goethite ore from Shanxi, China, and employs suspension reduction magnetization roasting–magnetic separation to investigate iron recovery. The effects of feed particle size, roasting temperature, roasting time, and CO concentration on iron grade and recovery are systematically examined to determine the preferred process parameters within the tested ranges. Combined with thermodynamic analysis of the Fe–O–C system, chemical phase analysis of iron, XRD, and SEM-EDS characterization, the thermodynamic laws and phase evolution mechanisms governing the directional transformation of hematite and goethite into magnetite are revealed. The results can provide a theoretical basis and technical support for the efficient beneficiation of high-alumina refractory hematite–goethite ores and the development of suspension magnetization roasting processes.

## 2. Materials and Methods

### *2.1. Materials*

The iron ore sample used in this study was collected from a representative sedimentary-weathered crust type Shanxi-type iron deposit in Jiaokou County, Shanxi Province, China. To ensure its representativeness, the ore was extracted using a multi-point sampling method from different active mining faces and was thoroughly homogenized by coning and quartering. The as-received ore contained an initial TFe grade of 35.72% and was characterized by the fine dissemination of hematite and goethite within aluminum-bearing gangue, which is typical for the refractory high-alumina hematite–goethite ores found in this region. After sampling, the ore was crushed successively using a jaw crusher (Wuhan Exploration Machinery Factory, Wuhan, China) and a double-roll crusher (Wuhan Exploration Machinery Factory, Wuhan, China) and then screened with standard sieves (Xinxiang Bashan Aviation Technology Co., Ltd., Xinxiang, China) to obtain a −3 mm raw material. For the roasting experiments, the −3 mm raw ore was ground in a laboratory disc mill (Guiyang Exploration Machinery Factory, Guiyang, China). To prepare each required size class (−1.0 mm, −0.6 mm, −0.3 mm, and −0.15 mm), the ground product was separately screened to ensure that 100% of the material passed the target sieve, with the oversize material returned to the mill for further grinding (Figure S1). The "−0.30 mm" size class denotes the entire material passing the 0.30 mm sieve, rather than a narrow size fraction. The size fraction distribution rates and cumulative passing percentages for the −3 mm raw ore and the −0.30 mm roasting feed are provided in Table S1. A −0.074 mm sample was also prepared for mineralogical characterization.

### *2.2. Methods*

The experimental flowsheet employed in this study consisted of suspension reduction roasting, grinding, and magnetic separation, as shown in Figure S2. The suspension reduction roasting experiments were conducted in a laboratory-scale suspension roasting system, which is schematically illustrated in Figure S3. The system mainly comprised a vertical tube resistance furnace (Item 1), a quartz reaction tube (Item 2) with an upper main reaction chamber (Item 11, inner diameter: 50 mm, length: 140 mm) and a lower gas flow channel (Item 13, inner diameter: 25 mm, total length: 360 mm), a gas supply unit, and a temperature control system. A porous quartz frit (Item 10) was placed at the bottom to act as the gas distributor.

For each experiment, a hot charging method was employed. The furnace was preheated to the target temperature under $N_2$ flow, after which 15 g of the ore sample was rapidly

dropped into the reaction chamber. The total gas flow rate was maintained at 600 mL/min. Through the transparent quartz reaction tube, the sample bed was visually observed to expand and dynamically disperse under the upward gas flow, preventing particle agglomeration and ensuring excellent gas–solid contact in this dynamically expanded/fluidized regime. In this study, the conventional term "suspension roasting" is used to describe this dynamic gas–solid state, distinguishing it from static fixed-bed roasting. A thermocouple (Item 3) (Hefei Kejing Materials Technology Co., Ltd., Hefei, China) positioned at the center of the reaction chamber measured the ambient temperature. Upon sample loading, the chamber temperature experienced a brief drop due to the cold sample and required approximately 3 min to fully recover to the preset target temperature. A quartz wool filter at the gas outlet (Item 12) captured any entrained fine particles.

Before heating, high-purity $N_2$ was introduced to remove residual air from the system. The gas was switched from $N_2$ to the CO–$N_2$ gas mixture to initiate reduction roasting only after the target temperature was fully restored. The roasting time (e.g., 10 min) was strictly recorded from the moment the gas was switched to the CO–$N_2$ mixture, completely excluding the $N_2$ preceding heating period and the 3 min thermal recovery period. The CO and $N_2$ used had purities of no less than 99.5% and 99.2%, respectively. During reduction, the CO/$N_2$ ratio was adjusted according to the specific experimental conditions using volumetric flow controllers (Hefei Kejing Materials Technology Co., Ltd., Hefei, China), while the total gas flow rate was maintained constant at 600 mL/min, with CO and $N_2$ flow rates ranging from 60 to 300 mL/min and from 300 to 540 mL/min, respectively. All gas flow rates mentioned above refer to those at the reactor inlet. Owing to experimental limitations, the gas flow rates inside the reactor and at the outlet were not measured.

Upon completion of roasting, the sample was cooled to room temperature under $N_2$ protection to prevent re-oxidation. The roasted products were subsequently ground in a laboratory three-roll, four-cylinder rod mill (Wuhan Exploration Machinery Factory, Wuhan, China) under wet grinding conditions at a pulp density of approximately 50 wt.%. The grinding time was controlled at 10 min to achieve the target fineness, and the achieved grinding fineness for all single-factor series is detailed in Table S2, confirming a final fineness of 85% passing 0.074 mm.

The ground slurry was subjected to magnetic separation using a Davis magnetic tube (Wuhan Exploration Machinery Factory, Wuhan, China). The entire roasted product (approximately 12–13 g) was used for each test. The magnetic flux density was set to 0.165 T (1650 G). The Davis tube was operated manually with a standard stroke motion. Washing was performed under a fixed water flow condition (preset on the apparatus) to ensure consistent removal of non-magnetic entrained particles. The magnetic concentrate and tailings were filtered, dried at 105 °C to a constant weight, weighed, and chemically analyzed. The overall iron recovery ($R_{Fe}$) was calculated based on the dry mass of the raw ore and the final concentrate using the following equation [30]:

$$R_{Fe}(\%) = 100 \times \frac{m_{concentrate}\, w_{concentrate}}{m_{raw}\, w_{raw}}, \quad (1)$$

where $R_{Fe}$ is the overall iron recovery from the raw ore to the final concentrate (expressed as a percentage), $m_{concentrate}$ and $m_{raw}$ are the dry masses of the final concentrate and the raw ore, and $w_{concentrate}$ and $w_{raw}$ are the corresponding iron mass fractions (grades). The head grade of the raw ore ($w_{raw}$ = 35.72%) was directly measured by chemical titration, not reconstructed from products. Detailed measured masses and assays for the raw ore, roasted product, concentrate, and tailings are provided in the closed mass balance in the Supplementary Materials, which represents the average values of three independent process replicates under the preferred conditions. Because the roasting process only involves the removal of volatile components (LOI and oxygen) without physical iron rejection, the

overall recovery from raw ore to concentrate is the most industrially relevant metric. The magnetic separation-stage recovery could be calculated using the roasted feed mass but is not reported here as it does not reflect the total iron recovery from the original ore.

To ensure the reliability of the results, each condition point in the single-factor experiments was evaluated through three independent process replicates ($n = 3$). Analytical replication and process replication are distinguished. The experimental results are presented as the mean ± standard deviation (SD). Analytical replication (e.g., repeated chemical titrations of the same sample) was performed to ensure measurement precision, which is distinct from the process. It should be noted that the analytical uncertainty (RSD < 5%) is significantly smaller than the process variability (represented by the SD of the three independent runs). Therefore, the differences between experimental conditions observed in the subsequent experiments are primarily governed by the process parameters. The effects of the main parameters were investigated sequentially via single-factor experiments. The preferred conditions reported herein represent the best conditions identified within the tested ranges, rather than a global optimum derived from a multivariable experimental design.

### *2.3. Measurement and Characterization*

X-ray diffraction (XRD, ULTIMA IV, Rigaku Corporation, Akishima, Tokyo, Japan) was employed to characterize the structural properties of the samples. The instrument was operated with Cu Kα radiation at 40 kV and 40 mA, scanning from 5° to 70° (2θ) with a step size of 0.02°. Phase identification was performed using the ICDD PDF-4+ database. Scanning electron microscopy coupled with energy-dispersive X-ray spectroscopy (SEM–EDS; Sigma 300, Carl Zeiss Microscopy GmbH, Jena, Germany; EDAX, XFlash 6/60, Bruker Nano GmbH, Berlin, Germany) was used to examine the morphology, elemental composition, and elemental distribution of the samples. The SEM was operated at an accelerating voltage of 20 kV with a working distance of 9.0 mm, utilizing a backscattered electron (BSE) detector for imaging and an EDS detector for elemental mapping.

The metal concentrations of the samples were determined using inductively coupled plasma-optical emission spectrometry (ICP-OES, Avio 550, PerkinElmer, Waltham, MA, USA). Prior to analysis, samples were completely digested using a multi-acid mixture (HCl–$HNO_3$–HF–$HClO_4$). Calibration curves were established using certified standard solutions, and reagent blanks were subtracted. Certified reference materials (e.g., GBW07123) were analyzed alongside the samples to verify analytical accuracy, with spike recoveries ranging from 95% to 105%. The total iron content was determined by potassium dichromate titration (GB/T 6730.5-2022 [31]), with the titrant standardized using high-purity iron wire prior to analysis.

The standard Gibbs free energy data used for thermodynamic calculations were obtained from the FactPS and FToxid databases [32].

The chemical phase analysis of iron in the raw ore and roasted products was conducted using a standard five-phase separation method for iron ores (DZG 20.01-2011 (Rock and Mineral Analysis, 4th ed.)) [33]. The total iron content was determined to verify the mass balance of the separated phases. Briefly, a 0.5–1 g sample was first subjected to magnetic separation to isolate the magnetic iron fraction (magnetite and pyrrhotite), which was subsequently dissolved in HCl and titrated with potassium dichromate after $SnCl_2$ reduction. The non-magnetic fraction was then sequentially leached to separate the remaining phases: (1) iron carbonate (siderite) was extracted using a 2 mol/L acetic acid solution in a boiling water bath; (2) iron oxide (hematite and goethite) was dissolved in a 4 mol/L HCl solution containing $SnCl_2$; (3) iron sulfide was decomposed using aqua regia; and (4) the final residue was fused with $Na_2O_2$ to determine silicate iron. The iron contents in the acetic acid and $SnCl_2$–HCl leachates were determined by potassium dichromate titration, while

those in the aqua regia and $Na_2O_2$ fusion solutions were measured using sulfosalicylic acid spectrophotometry. Standard reference materials were used for quality control, and the relative standard deviation was below 5%. All analytical uncertainties (including an RSD of <5% for phase analysis and <1% for total iron titration) were propagated into the final iron distribution and recovery calculations, confirming that the measured differences between test conditions exceed the analytical error margins.

## 3. Results

### *3.1. Mineralogical Characteristics of the Raw Ore*

The chemical composition and iron phase distribution of the raw ore were presented in Tables 1 and 2, respectively. The chemical composition in Table 1 provides quantitative mass fractions, which serve as the basis for evaluating the mass balance and phase distributions. As shown in Table 1, the total iron (TFe) grade of the ore was 35.72%, indicating that the ore was a typical low-grade iron ore resource [34,35]. The FeO content was only 0.83%, suggesting that iron predominantly occurred as ferric iron minerals. The ore contained relatively high levels of $Al_2O_3$ (14.56%) and $SiO_2$ (14.66%), indicating that it was a high-alumina refractory iron ore [35]. The Loss on Ignition (LOI) was 9.88%, which can be primarily attributed to the dehydration of goethite and the dehydroxylation of kaolinite and diaspore [36]. In addition, the contents of harmful impurities such as sulfur and phosphorus were comparatively low.

**Table 1.** Results of chemical multi-element analysis of raw ore (%).

| Component | TFe | FeO | $TiO_2$ | $SiO_2$ | $Al_2O_3$ | CaO | LOI |
|---|---|---|---|---|---|---|---|
| Content | 35.72 | 0.83 | 1.07 | 14.66 | 14.56 | 1.96 | 9.88 |
| Component | S | P | Cu | Co | MgO | Ni | |
| Content | 0.41 | 0.12 | 0.11 | 0.019 | 0.40 | 0.11 | |

Note: Table 1 reports a combination of elemental (e.g., TFe) and oxide (e.g., FeO) quantities. Due to chemical overlap, these components are not intended to sum to 100%. The LOI is provided separately. All values are reported on a dry basis. TFe was determined using potassium dichromate titration, while other elements were measured via ICP-OES. The relative standard deviation (RSD) for all measurements is less than 5%.

**Table 2.** Results of chemical phase analysis of iron in raw ore (%). Phase separation: DZG 20.01-2011; total iron determination for mass-balance verification: GB/T 6730.5-2022. RSD < 5%.

| Phase | Hematite–Goethite Fe | Silicate Fe | Sulfide Fe | Carbonate Fe | Magnetite–Pyrrhotite Fe | Total |
|---|---|---|---|---|---|---|
| Content | 34.52 | 0.62 | 0.47 | 0.078 | 0.03 | 35.72 |
| Distribution | 96.65 | 1.74 | 1.32 | 0.22 | 0.08 | 100.00 |

The iron phase analysis results further revealed the occurrence characteristics of iron in the ore. As shown in Table 2, 96.65% of the total iron was distributed in hematite–goethite phases, whereas only minor amounts of iron occurred as silicate iron (1.74%), sulfide iron (1.32%), carbonate iron (0.22%), and magnetite-associated iron (0.08%). The extremely low proportion of naturally occurring magnetic iron minerals indicated that direct magnetic separation was ineffective for iron recovery. Therefore, converting weakly magnetic hematite and goethite into strongly magnetic magnetite through reduction roasting was essential for subsequent magnetic separation. The combined chemical and phase analysis results demonstrated that the ore was characterized by low iron grade, high alumina content, and the predominance of weakly magnetic iron-bearing phases, which collectively contributed to its refractory beneficiation behavior [34,35].

It should be noted that direct magnetic separation of the raw ore was not performed in this study. However, the iron phase analysis (Table 2) clearly shows that 96.65% of the total iron in the raw ore is hosted in weakly magnetic hematite and goethite, with only 0.08% in the magnetic fraction. Given the fine dissemination of these weakly magnetic phases, direct physical separation would be highly inefficient, which theoretically justifies the necessity of the reduction roasting step prior to magnetic separation [28,37].

The mineralogical composition of the raw ore was investigated using XRD, and the corresponding diffraction pattern is presented in Figure 1. The results indicated that the major iron-bearing minerals were hematite (α-$Fe_2O_3$) and goethite (α-FeOOH), while the gangue minerals mainly consisted of kaolinite and diaspore. No obvious diffraction peaks corresponding to magnetite were detected, which was consistent with the iron phase analysis results. The coexistence of hematite and goethite suggested that the ore was a typical hematite–goethite-associated iron ore. Moreover, the abundant presence of kaolinite and diaspore indicated the high-alumina nature of the ore. These gangue minerals were intimately intergrown with the iron-bearing phases, making them difficult to remove by conventional physical beneficiation methods. It should be noted that the XRD analysis provides qualitative mineral phase identification, and the relative peak intensities reflect crystallinity rather than absolute mass fractions. Although calcite ($CaCO_3$) exhibits strong diffraction peaks, the low CaO content in Table 1 suggests that the proportion of calcite in the ore is low. During roasting, the thermal decomposition of calcite contributes to the mass loss (LOI) and the generation of $CO_2$.

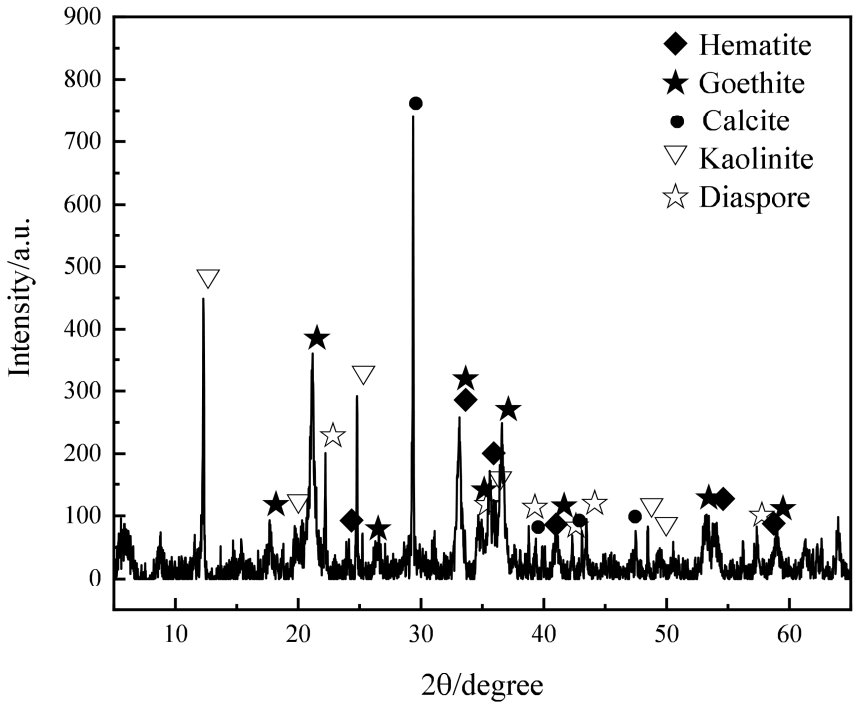



**Figure 1.** X-ray diffraction (XRD) pattern of the raw ore. The symbols denote the identified mineral phases: ◆ Hematite (α-$Fe_2O_3$), ★ Goethite (α-FeOOH), ● Calcite ($CaCO_3$), ▽ Kaolinite ($Al_2Si_2O_5(OH)_4$), and ☆ Diaspore (AlO(OH)).

To further investigate the textural characteristics and the disposition of various minerals, SEM-EDS analysis was conducted, and the results are presented in Figure 2. In the Backscattered Electron (BSE) image (Figure 2a), the atomic number contrast clearly delineates the mineral phases: the bright phases correspond to the iron-bearing minerals (hematite and goethite), while the dark grey areas represent the gangue, including alu-

minosilicates (e.g., kaolinite) and aluminum oxyhydroxides (e.g., diaspore). It is evident that hematite and goethite are finely disseminated and intimately intergrown with the gangue matrix. The irregular grain boundaries and complex interlocking textures indicate that a high degree of liberation is required to separate the iron minerals. EDS elemental mapping (Figure 2b,c) showed that Fe was predominantly enriched in the bright Fe-rich phases, whereas Si and Al were mainly concentrated within the dark grey gangue matrix. Such complex intergrowth characteristics were responsible for the poor beneficiation performance of the raw ore and highlighted the necessity of phase transformation through reduction magnetization roasting.

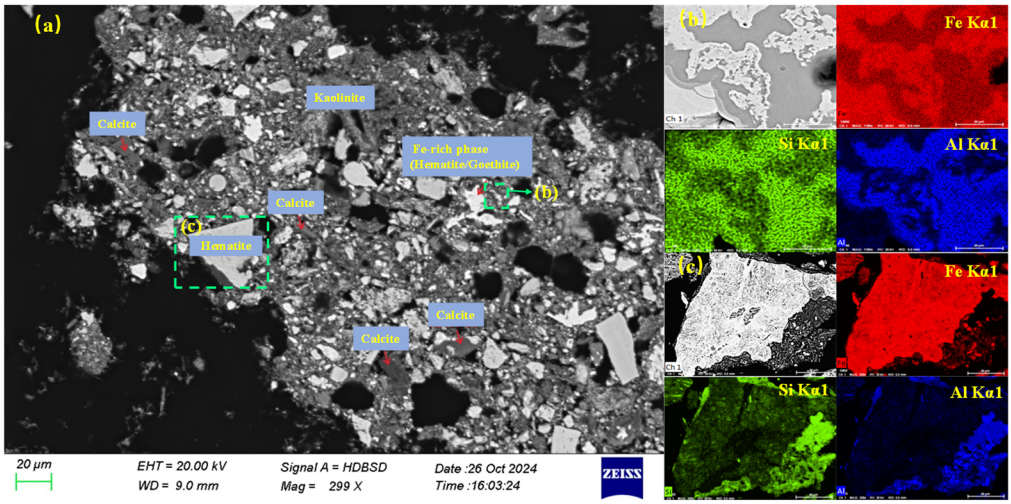



**Figure 2.** SEM–EDS analysis of the raw ore. The SEM images were acquired using a Sigma 300 field emission scanning electron microscope (Carl Zeiss Microscopy GmbH, Jena, Germany). (**a**) Backscattered electron (BSE) image showing the micro-texture and mineral associations (bright phases: Fe-rich phases; dark grey phases: gangue). The dashed boxes indicate the specific regions selected for EDS mapping: (**b**) a fine-grained Fe-rich phase area, and (**c**) a dense, large hematite grain. (**b**,**c**) EDS elemental mapping images showing the distribution of Fe (red), Si (green), and Al (blue). Note that EDS mapping provides qualitative elemental information, and the specific mineral phases were identified using XRD and chemical phase analysis.

### *3.2. Thermodynamic Analysis of Iron Oxide Phase Transformation*

The major iron-bearing minerals in the refractory hematite–goethite ore were hematite ($Fe_2O_3$) and goethite (FeOOH). During suspension reduction magnetization roasting, carbon monoxide acted as the reducing agent, and the reduction of iron oxides proceeded through a stepwise reduction pathway from higher-valence oxides to lower-valence phases [38,39]. Initially, goethite dehydrates to form hematite according to Equation (2) (shown in Table 3). Subsequently, hematite was reduced to magnetite, which could theoretically be further reduced to wüstite (FeO) and metallic iron (Fe) under strongly reducing conditions, as described by Equations (3)–(6) [40]. Based on simplified theoretical pathways, wüstite could react with reactive Si- and Al-bearing species (theoretically represented as $SiO_2$ and $Al_2O_3$) to form fayalite ($Fe_2SiO_4$) and hercynite ($FeAl_2O_4$) (Equation (7) shows the fayalite pathway) [41]. Fayalite was a weakly magnetic silicate phase and was difficult to recover by low-intensity magnetic separation; its formation would consume reduced iron species and increased iron losses in tailings. Hercynite formation, if it occurs, would similarly lock iron into a spinel phase with poor magnetic response. Therefore, maintaining a suitable degree of reduction is critical to promote the selective conversion of hematite and goethite into magnetite while suppressing over-reduction. In this study, although FeO was not directly identified using XRD in the roasted products, its potential formation is treated

strictly as a possible metastable intermediate or an unverified explanation for the observed deterioration in magnetic separation performance under strong reducing conditions.

**Table 3.** Main chemical Equations during suspension reduction magnetization roasting.

| Equations | Number |
|---|---|
| $2FeOOH \rightarrow Fe_2O_3 + H_2O$ | (2) |
| $3Fe_2O_3 + CO \rightarrow 2Fe_3O_4 + CO_2$ | (3) |
| $Fe_3O_4 + CO \rightarrow 3FeO + CO_2$ | (4) |
| $FeO + CO \rightarrow Fe + CO_2$ | (5) |
| $Fe_3O_4 + 4\,CO \rightarrow 3Fe + 4\,CO_2$ | (6) |
| $2FeO + SiO_2 \rightarrow Fe_2SiO_4$ | (7) |

Note: These equations represent simplified theoretical pathways. The actual reactive Si- and Al-bearing phases exist as complex minerals (e.g., kaolinite, diaspore) with activities less than unity. Hercynite is not included here as its formation was not experimentally verified.

To clarify the thermodynamic mechanism governing iron mineral transformation, the standard Gibbs free energy changes ($\Delta G°$) of Equations (2)–(7) were calculated using standard thermodynamic data from the FactPS and FToxid databases [32]. The complete analytical derivation is detailed in Table S3a,b. The standard states are defined as pure solids with unit activity (a = 1) and ideal gases at p° = 1 bar. In the FToxid database, wüstite is modeled as a nonstoichiometric solid solution phase ($Fe_{1-x}O$) rather than a strictly stoichiometric compound. The calculated $\Delta G° - T$ relationships are presented in Figure 3a, and the numerical values are provided in Supplementary Table S3a,b.

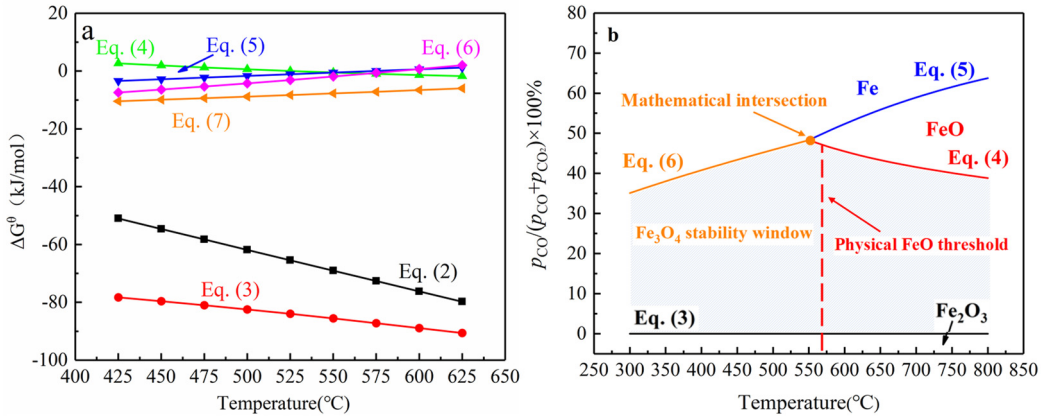



**Figure 3.** Thermodynamic analysis of iron oxide reduction in the Fe–O–C system: (**a**) standard Gibbs free energy changes ($\Delta G°$) of Equations (2)–(7), reported per mole of reaction as written (see Supplementary Table S3a,b for numerical values); (**b**) predominance diagram showing the equilibrium stability regions as functions of temperature and $x = p_{CO}/\left(p_{CO} + p_{CO_2}\right) \times 100\%$. The shaded area schematically indicates the $Fe_3O_4$ stability window; its lower and upper boundaries are defined by Equations (3), (4) and (6), respectively. The mathematical boundaries of Equations (4)–(6) converge at ~550 °C, whereas ~570 °C marks the physical eutectoid decomposition temperature of bulk FeO. Equation (6) is relevant below ~570 °C, where bulk FeO is not stable, and Equation (4) is relevant above this temperature. The ordinate is the equilibrium $CO/(CO + CO_2)$ ratio, not the inlet CO volume fraction in a CO–$N_2$ mixture. Because the outlet $CO/CO_2$ ratio was not measured, the experimental inlet conditions cannot be directly plotted on this diagram; the diagram is used only as a qualitative thermodynamic reference.

It must be emphasized that the tabulated $\Delta G°$ values are reported per mole of reaction as written according to the stoichiometric coefficients in Table 3 (i.e., the value for Equation (3) corresponds to the overall free energy change for 3 mol of $Fe_2O_3$ and 1 mol of

CO; the value for Equation (6) corresponds to 1 mol of $Fe_3O_4$ and 4 mol of CO). Within the experimental temperature range (425–625 °C), the dehydration of goethite (Equation (2)) and the reduction of hematite to magnetite (Equation (3)) possess strongly negative $\Delta G°$ values (ranging from approximately −50 to −90 kJ/mol), indicating standard-state feasibility. In contrast, the $\Delta G°$ values for the reduction of magnetite to wüstite (Equation (4)) are positive at lower temperatures (2.72 kJ/mol at 425 °C) and become negative at higher temperatures, crossing zero around 550 °C. Furthermore, the $\Delta G°$ values for the reduction of wüstite to metallic iron (Equation (5)) and the direct reduction of magnetite to metallic iron (Equation (6)) are slightly negative at lower temperatures but become positive toward the upper end of the temperature range (crossing zero at ~575 °C and ~600 °C, respectively). Equation (7) shows moderately negative $\Delta G°$ values (between −5.94 and −10.39 kJ/mol).

In summary, standard-state calculations indicate that the iron oxides undergo a sequential transformation of FeOOH → $Fe_2O_3$ → $Fe_3O_4$ during suspension roasting. However, it is important to distinguish between standard-state thermodynamic favorability and the actual reaction conditions. The actual Gibbs free-energy change is $\Delta G = \Delta G° + RT\ln Q$, where $Q$ is the reaction quotient under the prevailing gas composition. For the ideal gas–solid system, the reaction quotients are defined as $Q = p_{CO_2}/p_{co}$ for Equations (3)–(5), and $Q = \left(p_{CO_2}/p_{co}\right)^4$ for Equation (6); for Equation (2), $Q = p_{H_2O}$. Although deep reduction to metallic iron (Equations (5) and (6)) can be thermodynamically feasible at lower temperatures, the actual formation of metallic iron in the reactor is further suppressed by the increasing reaction quotient $Q$ due to $CO_2$ accumulation in the actual gas atmosphere. Meanwhile, metallic iron generation is also effectively constrained by the kinetic limitations of the short residence time and the competitive formation of $Fe_2SiO_4$ (Equation (7)). It must be emphasized that stable bulk wüstite is not an equilibrium phase below approximately 570 °C; below this temperature, it undergoes eutectoid decomposition to Fe and $Fe_3O_4$ [42]. However, this does not preclude the possibility of metastable or transient wüstite formation under kinetic control [43]. Consequently, while stable wüstite is largely absent (thus limiting the precursor for fayalite formation), transient FeO could potentially act as a precursor for minor fayalite formation under highly localized reducing conditions, though this remains a theoretical possibility [44,45].

To further evaluate the phase stability of iron oxides from a thermodynamic perspective, a predominance area diagram of the Fe–O–C system was constructed based on the principle of Gibbs free energy minimization (Figure 3b). The diagram illustrates the stability boundaries among hematite, magnetite, wüstite, and metallic iron as functions of temperature and the gas ratio $x = p_{CO}/\left(p_{CO} + p_{CO_2}\right) \times 100\%$. The equilibrium boundary $x$ as a function of temperature was derived using the relation $x = \frac{1}{\left[1+\exp\left(-\frac{\Delta G^\circ}{nRT}\right)\right]} \times 100\%$, where $n$ is the stoichiometric coefficient of the gas-phase species in the respective reaction (e.g., $n = 1$ for Equation (4), and $n = 4$ for Equation (6)). Based on this derivation, the theoretical magnetite stability window varies with temperature. At 500 °C, the $Fe_3O_4$/Fe equilibrium (Equation (6)) corresponds to $x \approx 45.9\%$, whereas the metastable $Fe_3O_4$/FeO boundary (Equation (4)) lies near $x \approx 52.5\%$. Because bulk wustite is not stable below approximately 570 °C, Equation (6) is the relevant upper boundary for magnetite under equilibrium at 500 °C; the magnetite field extends from the $Fe_2O_3$/$Fe_3O_4$ boundary (Equation (3), $x$ close to 0) to this upper boundary. As the temperature increases to approximately 550 °C, the theoretical equilibrium boundaries of Equations (4)–(6) mathematically converge at $x \approx 48.3\%$. However, it must be noted that 570 °C is the physical eutectoid decomposition temperature of bulk wustite (4FeO → $Fe_3O_4$ + Fe) [42]. Therefore, below the physical threshold of 570 °C, stable bulk FeO cannot exist, and Equation (6) remains the relevant upper boundary for magnetite even if the mathematical curves intersect at 550 °C. Above 570 °C, stable wustite can appear and Equation (4) becomes the relevant $Fe_3O_4$/FeO bound-

ary. The diagram indicates that magnetite possesses a relatively broad stability region under moderate temperatures and relatively weak reducing potentials.

Furthermore, the reactive Si- and Al-bearing phases in the raw ore (e.g., kaolinite and diaspore) do not exist as pure free $SiO_2$ or $Al_2O_3$, meaning their actual activities are less than unity. Therefore, the reactions shown in Table 3 (e.g., Equation (7)) represent simplified theoretical pathways. The formations of fayalite and hercynite are treated strictly as possible side reactions that are thermodynamically favored under strong reducing conditions, rather than demonstrated mechanisms in this study [46]. Although hercynite can form as a solid solution between magnetite and reactive alumina species, its formation is kinetically limited at low temperatures and requires the sustained presence of magnetite as a host phase and sufficient chemical activity of Al [47]. No additional reaction for hercynite has been added to Table 3, as a balanced equation alone would not establish its occurrence without direct phase-sensitive evidence.

It is important to distinguish between standard-state thermodynamic favorability and the actual reaction conditions. The actual Gibbs free-energy change is $\Delta G = \Delta G^\circ + RT\ln Q$, where $Q$ is the reaction quotient under the prevailing gas composition. It should be noted that because the stoichiometric coefficients differ, their absolute $\Delta G^\circ$ magnitudes cannot be directly compared to identify a dominant transformation step, although the tabulated values are consistently reported per mole of reaction as written.

It should be strongly emphasized that the predominance area diagram is defined in terms of the equilibrium gas ratio $x = p_{CO}/(p_{CO} + p_{CO_2}) \times 100\%$, rather than the inlet CO volume fraction in a CO–$N_2$ mixture. For a CO–$N_2$ feed with negligible inlet $CO_2$, the initial value of this variable is close to 100%, not 30% or 45% [48]. Therefore, the inlet CO concentrations of 30 vol.%–45 vol.% used in this work are empirical process conditions and cannot be directly mapped onto a specific position in Figure 3b [29]. Because the outlet $CO/CO_2$ ratio was not measured, the actual local oxygen potentials and the reaction path cannot be reconstructed. Consequently, the experimental conditions should not be described as falling within the magnetite stability region solely based on the inlet CO concentration. Nevertheless, the experimental results are consistent with the general thermodynamic trend that moderate temperatures and weakly reducing atmospheres favor the selective conversion of hematite–goethite to magnetite, thereby avoiding the formation of detectable over-reduced phases.

### *3.3. Effect of Suspension Roasting Parameters*

Figure 4a shows the effect of feed particle size on the magnetic separation performance of the roasted products. Both the concentrate grade and iron recovery initially increased and then decreased with decreasing particle size, reaching preferred values at −0.30 mm, where a concentrate iron grade of 56.77% and an iron recovery of 86.26% were obtained. At coarse particle sizes (−1.0 mm), the limited specific surface area and long diffusion path hindered gas penetration and heat transfer, resulting in incomplete reduction of hematite and goethite. Reducing the particle size to −0.30 mm significantly enhanced gas–solid contact and promoted uniform suspension roasting, thereby facilitating the conversion of weakly magnetic iron oxides into magnetite. However, further size reduction to −0.15 mm slightly decreased iron recovery. This decline might be attributed to particle agglomeration and local over-reduction, which may have led to the formation of weakly magnetic FeO, as has been reported in other magnetizing roasting studies [25,49]. Nevertheless, direct evidence for agglomeration and FeO formation under this specific condition was not obtained in the present work; these remain speculative explanations, and further investigation is warranted. Therefore, −0.30 mm was selected as the preferred feed size within the tested range.

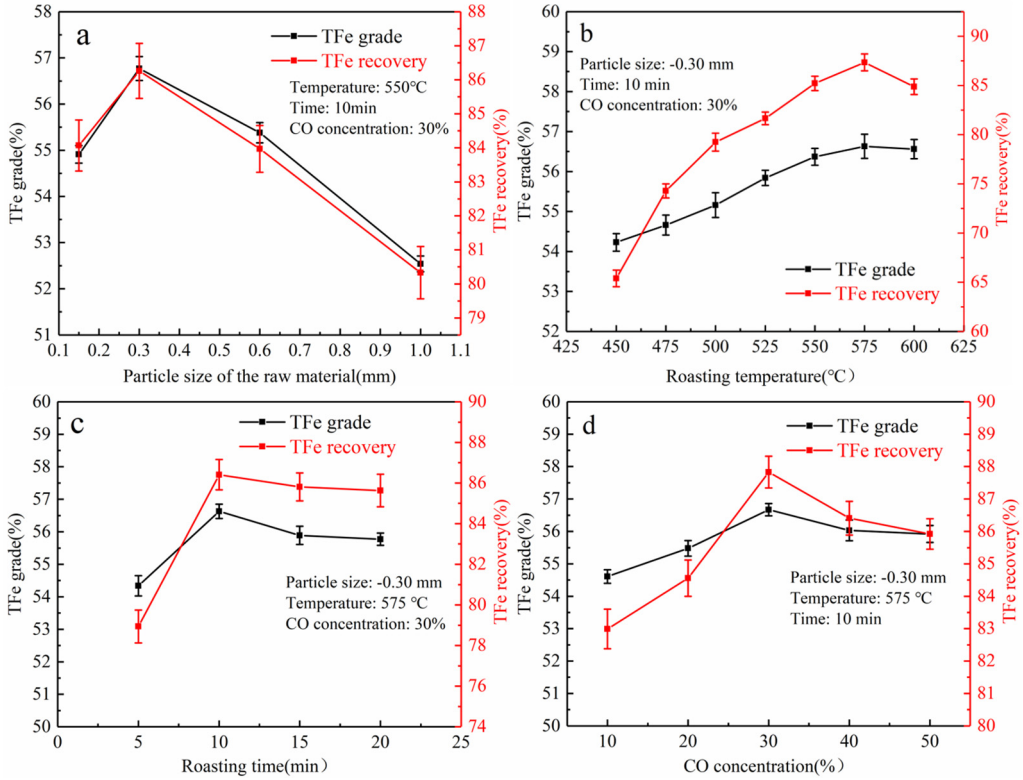



**Figure 4.** Effects of different roasting parameters on the TFe grade and TFe recovery of magnetic concentrate: (**a**) feed particle size (fixed at 550 °C, 10 min, 30% CO); (**b**) roasting temperature (fixed at −0.30 mm, 10 min, 30% CO); (**c**) roasting time (fixed at −0.30 mm, 575 °C, 30% CO); and (**d**) CO concentration (fixed at −0.30 mm, 575 °C, 10 min). Data are presented as mean ± standard deviation (SD) of three independent experiments ($n = 3$) for each condition point. Note that the center point conditions were independently repeated across the temperature, time, and CO concentration series.

The effect of roasting temperature is shown in Figure 4b (experimental tested range: 450–600 °C). Both concentrate grade and iron recovery increased with temperature, reaching preferred values at 575 °C, with a concentrate iron grade of 56.63% and an iron recovery of 87.37%, followed by a decline at higher temperatures. At low temperatures (450–500 °C), the reduction of hematite and goethite proceeded slowly, resulting in insufficient magnetite formation. Increasing the temperature accelerated the reduction reaction. The preferred temperature of 575 °C is consistent with the general temperature-dependent thermodynamic stability window of magnetite (as discussed in Section 3.2). Further increasing the temperature might have promoted over-reduction of magnetite to FeO and the possible formation of fayalite ($Fe_2SiO_4$), which could deteriorate the magnetic separation performance [50]. However, these phases were not directly identified in the roasted products under the corresponding conditions in this study; thus, these explanations remain speculative. Consequently, 575 °C was identified as a suitable roasting temperature for subsequent single-factor experiments.

The influence of roasting time on magnetic separation performance was shown in Figure 4c. Both the concentrate iron grade and iron recovery increased markedly as the roasting time increased from 5 to 10 min, rising from 54.34% and 78.94% to 56.63% and 86.41%, respectively; thereafter, the values remained relatively stable within the standard deviation. A roasting time of 5 min was insufficient for complete reduction of hematite and goethite, resulting in limited magnetite formation. Extending the roasting time to 10 min enabled a more complete phase transformation and produced more favorable separation performance. Further prolonging the roasting time to 15 min showed no statistically significant

improvement in recovery, but a marginal decrease in the concentrate grade, which might be associated with partial over-reduction of newly formed magnetite [39]. However, direct phase-sensitive evidence was not obtained to confirm this phenomenon. Considering both metallurgical performance and process efficiency, a roasting time of 10 min was adopted for the subsequent condition screening.

It should be emphasized that the preferred 575 °C/10 min condition is a deliberate engineering trade-off between thermodynamic phase stability and kinetic reaction rates. Thermodynamically, bulk wustite is unstable below approximately 570 °C, which means operation at 550–560 °C would theoretically guarantee a pure magnetite product without any risk of over-reduction. However, at these lower temperatures, the reduction kinetics are sluggish, and a 10 min residence time is insufficient for the complete magnetization of hematite and goethite (as evidenced by the lower recovery at 450–550 °C in Figure 4b). By selecting 575 °C, the system crosses the 570 °C threshold just enough to achieve rapid and complete reduction within 10 min. Although this temperature technically permits FeO formation, the risk of over-reduction is effectively suppressed by the short residence time (10 min) and the moderate CO concentration (30%). The fully suspended state provides excellent gas–solid contact, which accelerates the reduction kinetics, making this short residence time sufficient for extensive magnetization [29]. Thus, 575 °C represents a deliberate trade-off for phase selectivity and energy efficiency.

Figure 4d illustrates the effect of CO concentration on the roasting performance. Both the concentrate grade and iron recovery first increased and then decreased with increasing CO concentration, with preferred values obtained at a CO concentration of 30%, where a concentrate iron grade of 56.67% and an iron recovery of 87.83% were achieved. At low CO concentrations, the reducing atmosphere was insufficient to achieve effective magnetization roasting, resulting in incomplete conversion of hematite and goethite. Increasing the CO concentration enhanced the reduction potential and promoted magnetite formation, thereby improving both the concentrate grade and recovery. However, at higher CO concentrations (e.g., 40%–50%), the reducing atmosphere was intensified, which might have favored the further reduction of magnetite to FeO, as predicted by the thermodynamic analysis [39]. This over-reduction could account for the slight decrease in the magnetic separation performance at excessive CO levels. However, since FeO was not directly identified in the roasted products, this explanation should be considered a possible mechanism rather than a demonstrated one. Therefore, a CO concentration of 30% was selected as the preferred reducing condition.

It should be noted that the data points at the nominal center conditions (−0.30 mm, 575 °C, 10 min, and 30% CO) appear independently across the temperature, time, and CO concentration series. Because these center points were tested in different experimental batches, their mean values exhibit slight variations (concentrate grade: 56.63%–56.67%; iron recovery: 86.41%–87.83%), reflecting the normal inter-batch variance of the process. These three runs collectively serve as internal confirmation experiments. For clarity and traceability, the specific values reported in the Abstract and Conclusions (56.67% grade and 87.83% recovery) correspond to the mean values of the three independent replicates in the CO concentration series (Figure 4d). The closed mass and iron balance in Table S4 are calculated directly using the arithmetic means of the mass and grade data from these three runs.

To quantitatively evaluate the rejection of gangue minerals, the chemical compositions of the concentrate and tailings were analyzed (Table S5). The results showed that the concentrate contained 7.41% $Al_2O_3$ and 8.87% $SiO_2$, compared to 35.76% $Al_2O_3$ and 26.79% $SiO_2$ in the tailings. Based on the concentrate mass balance, the rejection rates of $Al_2O_3$ and $SiO_2$ are calculated to be 71.83% and 66.50%, respectively. It should be noted that if

calculated based on the tailings assay, the $SiO_2$ rejection would be approximately 56.25%. The overall $SiO_2$ mass balance closes at approximately 89.7%. This slight non-closure is primarily attributed to unavoidable physical handling losses of ultra-fine gangue particles and analytical uncertainties (RSD < 5%). Nevertheless, these results confirm the effective separation of iron from the high-alumina gangue. The residual $Al_2O_3$ and $SiO_2$ in the concentrate are primarily attributed to the micro-scale intergrowth and gangue entrapment observed in subsequent SEM-EDS analysis.

Regarding the downstream application, the concentrate (56.67% Fe) with low S (0.26%) and P (0.08%) contents is potentially suitable as a blending feedstock for blast furnace ironmaking or for sintering/pelletizing, as the S and P levels fall below standard thresholds typically required for blast furnace/sintering feeds [51]. However, considering the residual $Al_2O_3$ (7.41%) and $SiO_2$ (8.87%) contents, further fine grinding and cleaning, or blending with high-grade ores, would be necessary to meet the strict thresholds for direct reduction iron (DRI) or specific smelting processes.

### *3.4. Phase Evolution and Transformation Mechanism*

To evaluate the phase transformation behavior of iron minerals under the preferred roasting conditions, the roasted product was subjected to iron phase analysis, and the results were summarized in Table 4. Compared with the raw ore (Table 2), a significant redistribution of iron among different mineral phases was observed after suspension reduction roasting. The distribution proportion of iron occurring in the hematite–goethite phases decreased dramatically from 96.65% in the raw ore to 5.71% after roasting, whereas the distribution proportion of iron occurring in the magnetic fraction (magnetite and pyrrhotite) increased sharply from only 0.08% to 92.07%. These results clearly demonstrated an extensive transformation of iron into the magnetic fraction during roasting. In contrast, the distribution of silicate-associated iron decreased from 1.74% to 0.82%. Although this is a small absolute change (0.92 percentage points), it represents a relative decrease of approximately 52.9%. It is important to distinguish this change in phase distribution from the change in overall Fe concentration caused by mass loss. The loss of structural water and oxygen during roasting increases the relative Fe concentration in the solid product, which would theoretically increase the absolute percentage of all Fe-bearing fractions. The observed decrease in the silicate-associated Fe fraction is therefore primarily attributed to physical encapsulation and phase reassignment during the analytical procedure. As newly formed magnetite grains encapsulate fine silicate gangue particles, these composite particles are physically dragged into the magnetic fraction during the initial magnetic separation step of the phase analysis. Consequently, the iron associated with these encapsulated silicates is misclassified into the magnetite/pyrrhotite fraction rather than the silicate fraction in the subsequent leaching steps. Given the low absolute abundance of silicate Fe and the analytical uncertainty (RSD < 5%), this relative change is highly sensitive to sample heterogeneity. Furthermore, on a consistent mass basis, the loss of volatile components (structural water and oxygen) during roasting alters the total mass. The apparent decrease may also arise from extraction behavior, as newly formed magnetite could encapsulate fine silicate gangue particles, reducing their extraction efficiency in the final $Na_2O_2$ fusion step [49]. Therefore, rather than implying that the silicate minerals were completely inert, this slight absolute decrease likely reflects a combination of analytical uncertainty and physical encapsulation, which does not alter the primary conclusion that the majority of iron was transformed into the magnetic fraction. It should be noted that the increase in the TFe grade of the roasted product (41.47%) compared to the raw ore (35.72%) is primarily attributed to the loss of structural water and oxygen (mass loss of 13.86%), as verified by the closed mass balance in Table S4, rather than physical gangue rejection. The substantial increase in magnetite

content indicated that suspension reduction roasting effectively enhanced the magnetic properties of the refractory hematite–goethite ore and created favorable conditions for subsequent magnetic separation.

**Table 4.** Results of chemical phase analysis of iron in the roasted product (%). Phase separation: DZG 20.01-2011; total iron determination for mass-balance verification: GB/T 6730.5-2022. RSD < 5%.

| Phase | Magnetite–Pyrrhotite Fe | Carbonate Fe | Hematite–Goethite Fe | Sulfide Fe | Silicate Fe | Total |
|---|---|---|---|---|---|---|
| Content | 38.18 | 0.05 | 2.37 | 0.53 | 0.34 | 41.47 |
| Distribution | 92.07 | 0.12 | 5.71 | 1.28 | 0.82 | 100.00 |

The mineralogical changes induced by roasting were further investigated using XRD analysis, and the diffraction patterns were presented in Figure 5. Compared with the raw ore, the roasted product exhibited pronounced changes in phase composition. The characteristic diffraction peaks of hematite and goethite were significantly weakened or even disappeared after roasting, whereas the diffraction peaks corresponding to magnetite became dominant. The emergence and strengthening of magnetite diffraction peaks indicated that the weakly magnetic iron oxides were extensively transformed into magnetic phases during suspension roasting. Meanwhile, the diffraction peaks of the major aluminosilicate gangue mineral (kaolinite) showed only minor changes in both position and intensity. Although the crystalline kaolinite did not show significant structural changes in the XRD pattern, it may have undergone dehydroxylation to form amorphous metakaolinite at the roasting temperature [52]. However, the exact extent of this dehydroxylation was not quantified in this study. Although the absence of labeled diaspore peaks in the roasted product might suggest a change, it does not prove a zero-phase content. The characteristic peaks of diaspore likely weakened or overlapped with other gangue phases, falling below the detection limit of XRD. Furthermore, it should be noted that both the preceding $N_2$ heating period and the 10 min roasting at 575 °C provided sufficient thermal history for potential dehydroxylation [52]. Overall, the XRD results provide qualitative and semi-quantitative phase identification and are consistent with the iron phase analysis, confirming an extensive transformation of hematite and goethite into magnetic phases under the preferred roasting conditions.

As shown in Figure 6, which presents the roasted product prior to magnetic separation, the backscattered electron images revealed that the material mainly consisted of bright Fe-rich particles surrounded by relatively dark aluminum-bearing gangue minerals. Elemental mapping indicated that Fe was highly concentrated within the magnetite particles, whereas Si and Al were predominantly distributed in the surrounding gangue matrix. While the elemental maps are qualitative and cannot uniquely identify mineral phases, when integrated with the XRD and chemical phase analysis results, the distinct phase boundaries between Fe-rich and Al/Si-rich regions suggested that the reduction roasting process effectively transformed hematite and goethite into magnetite without inducing extensive chemical incorporation of Al and Si into the iron-bearing lattice. This observation was consistent with the XRD results, in which no obvious iron silicate phases were detected. As shown in Figure 6b, the yellow circles highlight localized weak Si and Al signals observed within/around several magnetite particles, indicating that a minor amount of aluminum-bearing gangue remained locally entrapped or closely associated with the magnetite after roasting. It is highly likely that this local intergrowth was related to the original mineral texture rather than newly formed reaction products, although other spatial or analytical explanations (such as incomplete reduction or surface artifacts) cannot be entirely excluded based solely on these maps. Nevertheless, Fe remained the dominant

element within the magnetite particles, confirming that selective phase transformation and iron enrichment were accomplished during suspension reduction roasting.

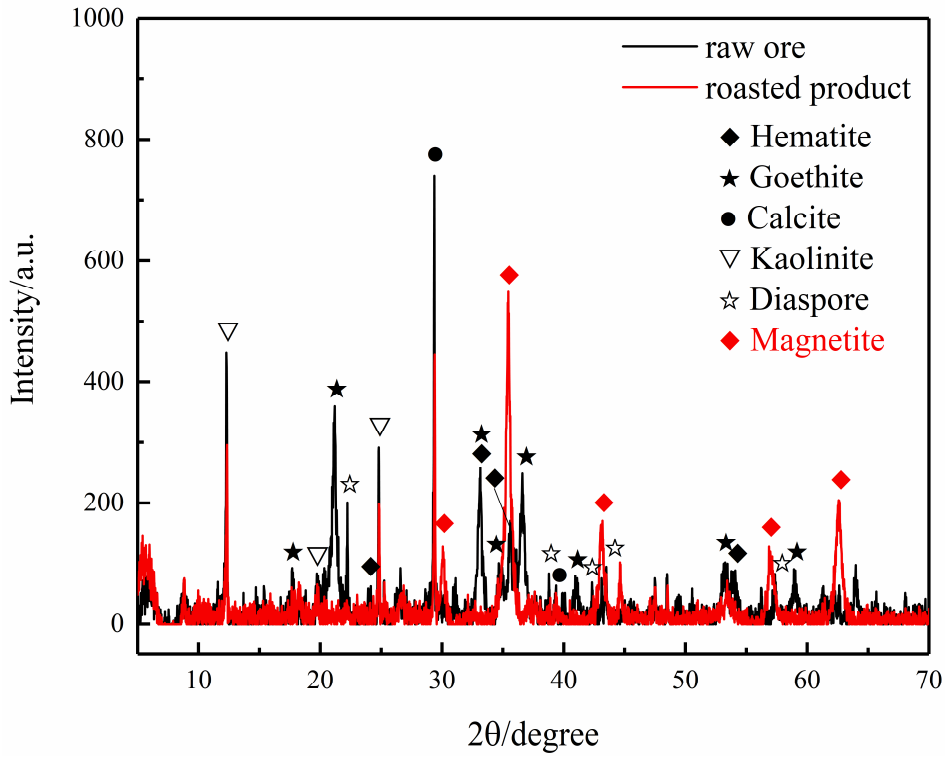



**Figure 5.** X-ray diffraction (XRD) patterns of the raw ore (black line) and the roasted product obtained under the preferred conditions (red line). The symbols denote the identified mineral phases: ◆ Hematite (α-$Fe_2O_3$), ★ Goethite (α-FeOOH), ● Calcite ($CaCO_3$), ▽ Kaolinite ($Al_2Si_2O_5(OH)_4$), ☆ Diaspore (AlO(OH)), and ◆ (red) Magnetite ($Fe_3O_4$).

Based on the thermodynamic analysis, iron phase analysis, XRD characterization, and SEM–EDS observations, a phase transformation mechanism for suspension reduction roasting was proposed and illustrated in Figure 7. It should be noted that the FeOOH → $Fe_2O_3$ → $Fe_3O_4$ sequence presented here is a chemically reasonable, literature-informed pathway, rather than an in situ time-resolved mechanism demonstrated in this study. During the initial stage of roasting, goethite underwent dehydration to form hematite. Subsequently, hematite was selectively reduced by CO to magnetite, which represented the desired magnetic phase for separation. Under the preferred roasting conditions, the reduction potential was sufficient to promote hematite to magnetite transformation while it remained below the threshold for extensive over-reduction. Meanwhile, the aluminum-bearing gangue domains (aluminosilicates such as kaolinite and aluminum oxyhydroxides such as diaspore) did not extensively react with the iron oxides to form new complex phases. However, it is acknowledged that dehydroxylation of kaolinite and diaspore may have occurred at the roasting temperature, potentially altering their original crystal structures into amorphous phases. As a result, the majority of iron was concentrated in the magnetite phase, whereas Al- and Si-bearing minerals remained in the nonmagnetic fraction. This selective phase transformation significantly enhanced the magnetic contrast between valuable minerals and gangue minerals. If the roasting temperature or reducing potential became excessive, magnetite might undergo further reduction to wüstite, which could subsequently react with Si- and Al-bearing species to form fayalite and hercynite. These over-reduction pathways, particularly the formation of hercynite, are treated strictly as literature-based hypotheses and are thermodynamically inferred; they were not directly identified in the

present products. If they occur, they would consume recoverable iron and potentially deteriorate magnetic separation performance. Therefore, maintaining an appropriate roasting atmosphere was essential for maximizing magnetite formation while kinetically and thermodynamically limiting undesirable secondary reactions. The combined experimental and thermodynamic results demonstrated that the efficient recovery of iron from the refractory hematite–goethite ore was primarily governed by the selective transformation of weakly magnetic hematite–goethite into strongly magnetic magnetite during suspension reduction roasting.

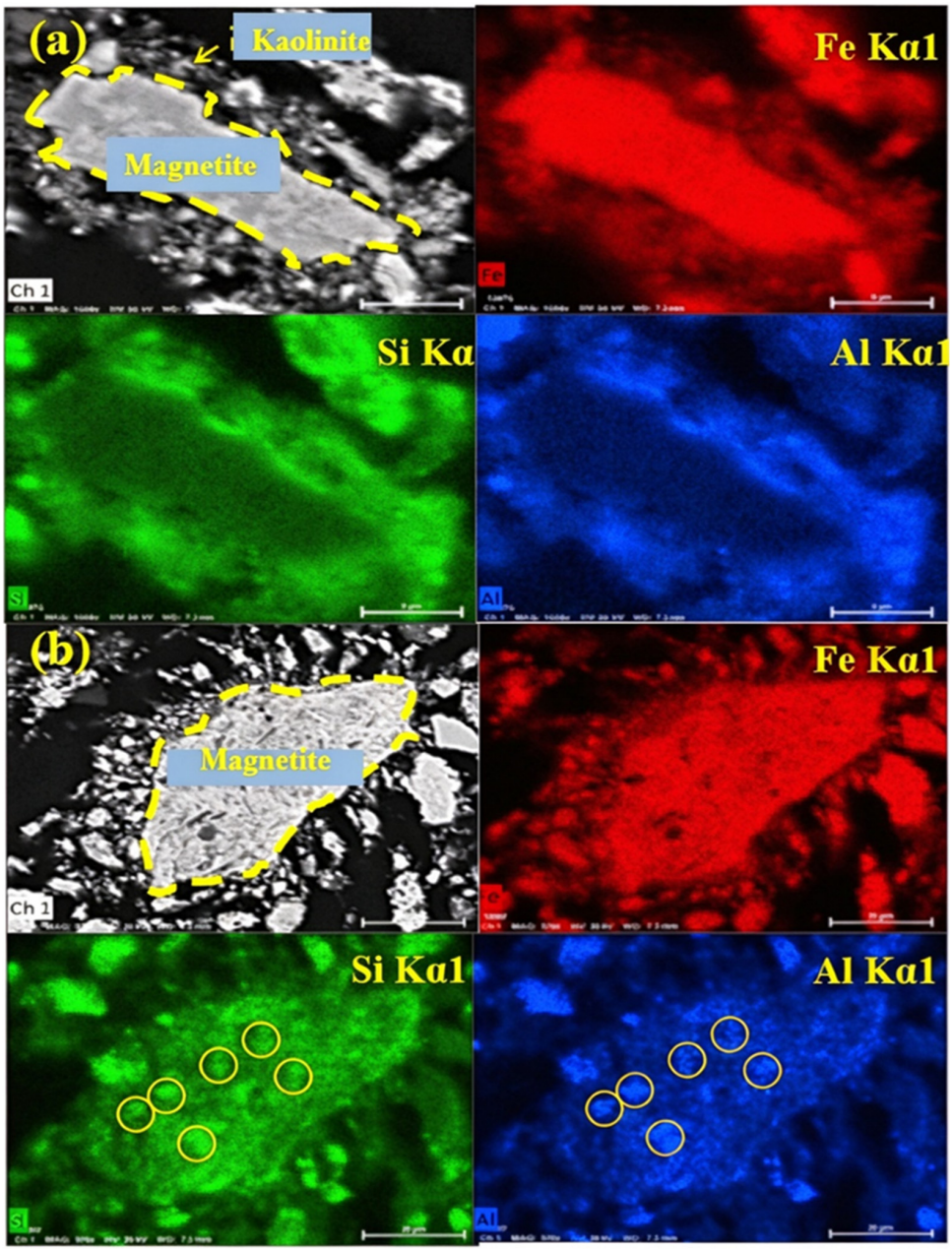



**Figure 6.** SEM–EDS analysis of the roasted product. (**a**,**b**) BSE images of different roasted particles showing the spatial relationship between the newly formed magnetite and the gangue matrix. The yellow dashed lines outline the magnetite grains, while the yellow solid circles highlight the localized weak Si and Al signals (indicating minor gangue entrapment). (Fe, red; Si, green; Al, blue). The scale bars in all subfigures of (**a**,**b**) represent 10 μm. Note that SEM–EDS provides qualitative elemental distribution, and phase identities are verified using XRD and chemical phase analysis.

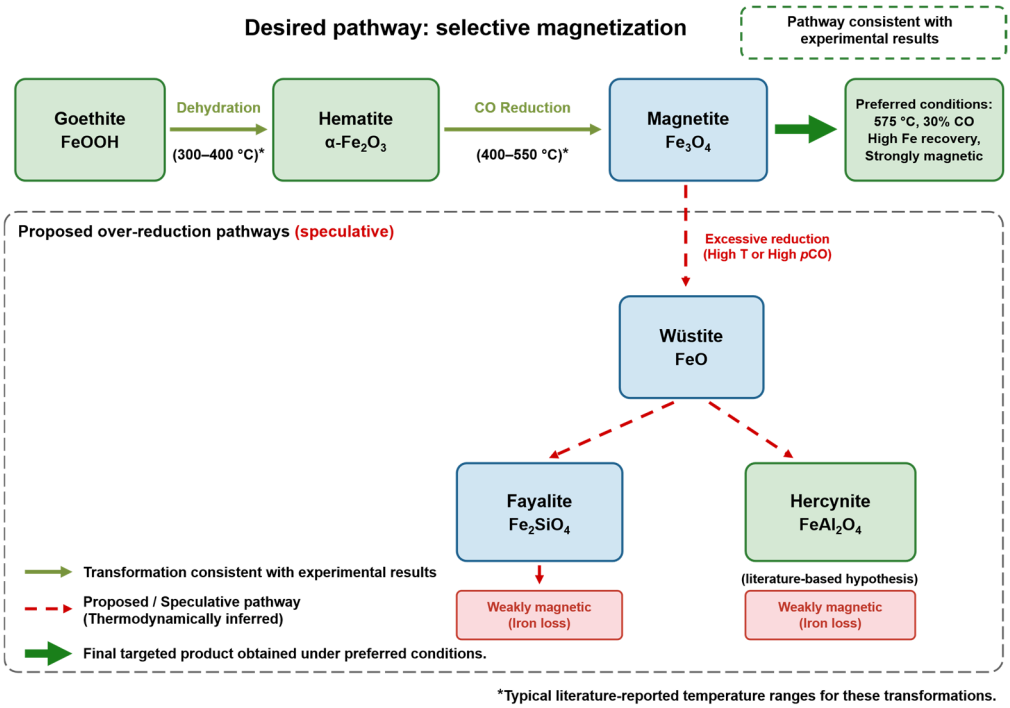



**Figure 7.** Schematic illustration of the proposed phase transformation pathways during suspension magnetization roasting. Solid green arrows denote the main transformation pathway (FeOOH → $Fe_2O_3$ → $Fe_3O_4$), which is directly supported by our experimental results (XRD, phase analysis, and magnetic separation). Dashed red arrows indicate the proposed over-reduction pathways ($Fe_3O_4$ → FeO → silicates/spinels), which are thermodynamically inferred and remain speculative. The large, thick green arrow on the right specifically highlights the final targeted product (magnetite) obtained under the preferred conditions, indicating that this pathway is consistent with our experimental findings. Direct phase identification for FeO, fayalite ($Fe_2SiO_4$), and hercynite ($FeAl_2O_4$) was not obtained in this work. The temperature intervals (300–400 °C and 400–550 °C, marked with *) represent typical literature-reported ranges for these transformations, rather than exact experimental thresholds measured in this specific reactor. The preferred empirical conditions (575 °C and 30% CO) were determined via single-factor screening experiments.

## 4. Conclusions

This study systematically investigated the recovery of iron from a refractory high-alumina hematite–goethite ore through suspension reduction roasting followed by magnetic separation. The effects of roasting parameters on magnetic separation performance were evaluated, and the phase transformation behavior of iron minerals was elucidated through thermodynamic calculations and multi-scale characterization. The main conclusions were summarized as follows:

(1) Suspension reduction roasting effectively improved the magnetic separation performance of the refractory hematite–goethite ore. Under the preferred conditions identified within the tested ranges (a feed particle size of −0.30 mm, a roasting temperature of 575 °C, a roasting time of 10 min, and a CO concentration of 30%), magnetic separation of the roasted ore yielded a concentrate with an Fe grade of 56.67% and a recovery of 87.83%. This demonstrates that appropriate roasting conditions are essential for efficient iron beneficiation.

(2) Thermodynamic analysis and experimental results revealed that selective magnetization was governed by the stability window of magnetite. Hematite and goethite could be readily reduced to magnetite within an appropriate temperature range and a moderate reducing atmosphere. Conversely, excessive temperatures or overly strong

reducing conditions may have promoted over-reduction, potentially leading to the formation of FeO, fayalite, and hercynite, which could deteriorate the magnetic separation performance. However, direct identification of these over-reduced phases requires further investigation.

(3) Iron phase analysis, XRD, and SEM–EDS characterization consistently indicated the selective phase transformation during suspension roasting. More than 92% of the iron was distributed in the magnetic fraction (magnetite and pyrrhotite), while the Al- and Si-rich gangue remained present in the nonmagnetic fraction after roasting. Although no new crystalline gangue phases were detected, the kaolinite component may have undergone partial dehydroxylation to form amorphous metakaolinite during the thermal process, though this extent was not quantitatively determined. The lack of chemical interlocking between Fe-rich and aluminum-bearing phases significantly enhanced the magnetic contrast between valuable minerals and gangue minerals.

(4) A phase transformation mechanism for suspension reduction roasting was proposed. The efficient recovery of iron was primarily governed by the selective transformation of hematite–goethite into magnetite, which follows a literature-informed FeOOH → $Fe_2O_3$ → $Fe_3O_4$ pathway. Under the preferred conditions, extensive over-reduction and the formation of iron silicates were not detected in the final product, consistent with their suppression under the preferred conditions. The findings provide both theoretical support and technical guidance for the efficient beneficiation of refractory high-alumina hematite–goethite ores.

Future work could also explore the application of rapid elemental characterization and supervised mineral classification (e.g., LIBS combined with machine learning [53]) for heterogeneous roasted products, although matrix-specific validation would be required.

**Supplementary Materials:** The following supporting information can be downloaded at: https://www.mdpi.com/article/10.3390/min16111193/s1, Figure S1: Preparation flow of the roasting feed materials. The −3 mm raw ore was ground in a disc mill and separately screened to pass the target sieve (1.0, 0.6, 0.3, or 0.15 mm). The oversize particles were returned for re-grinding, ensuring that 100% of the final sample passed the respective target sieve; Figure S2: Experimental process flow diagram for the recovery of iron from the high-alumina hematite-goethite ore using a laboratory-scale suspension roasting system; Figure S3: Schematic diagram of the laboratory-scale suspension roasting system. (1) Heating chamber; (2) Reaction tube; (3) Thermocouple; (4) Temperature controller; (5) Gas mixing tank; (6) Gas flow meter; (7) CO gas cylinder; (8) $N_2$ gas cylinder; (9) Gas inlet port; (10) Porous quartz frit; (11) Main reaction chamber (diameter: 50 mm, length: 140 mm); (12) Gas outlet port; (13) Gas flow channel (diameter: 25 mm, total length: 360 mm); Figure S4: Representative EDS spectra of the main mineral phases identified in the raw ore: (a) Fe-rich phase (hematite/goethite), showing dominant Fe and O peaks; (b) kaolinite, showing dominant Si, Al, and O peaks; (c) diaspore, showing dominant Al and O peaks; and (d) calcite, showing dominant Ca and O peaks; Table S1: Particle size distributions (fraction distribution rates and cumulative passing percentages) of the −3 mm raw ore and the −0.30 mm roasting feed; Table S2: Complete experimental matrix of the single-factor condition tests; Table S3a: Calculated standard enthalpy ($\Delta H$) and entropy ($\Delta S$) changes for reactions (2)–(7) at different temperatures (per mole of reaction as written); Table S3b: Calculated standard Gibbs free energy changes ($\Delta G°$), equilibrium constants ($K$), and equilibrium gas ratios ($x$) for reactions (2)–(7) at different temperatures.; Table S4: Closed dry-mass and iron balance for the raw ore, roasted product, concentrate, and tailings under the preferred roasting conditions (feed particle size of −0.30 mm, roasting temperature of 575 °C, roasting time of 10 min, and CO concentration of 30%); Table S5: Chemical composition of the roasted product, concentrate, and tailings under the preferred conditions (%).

**Author Contributions:** Conceptualization, C.C. and Y.Y.; methodology, Y.Y.; software, Z.Z.; validation, K.Z., Z.Z. and W.W.; formal analysis, K.Z.; data curation, K.Z. and W.W.; writing—original draft preparation, K.Z. and Z.Z.; writing—review and editing, K.Z. and C.C.; visualization, W.W.; project

administration, Y.Y.; funding acquisition, C.C. All authors have read and agreed to the published version of the manuscript.

**Funding:** This research was funded by the Deep Earth Probe and Mineral Resources Exploration-National Science and Technology Major Project, grant number 2024ZD1004000.

**Data Availability Statement:** The original contributions presented in this study are included in the article and its Supplementary Materials. Specifically, the particle size distributions (Table S1), detailed experimental matrix (Table S2), calculated thermodynamic data (Table S3a,b), closed mass and iron balances (Table S4), multi-element assays (Table S5), and representative EDS spectra (Figure S4) are available in the Supplementary Materials. The processed XRD patterns and phase identification parameters are provided in the main text. Raw instrument files (e.g., proprietary XRD and EDS binary formats) can be made available from the corresponding author upon reasonable request, subject to file size and software compatibility limitations.

**Acknowledgments:** The authors gratefully acknowledge the support from the Deep Earth Probe and Mineral Resources Exploration-National Science and Technology Major Project. The authors also sincerely thank the staff of the Institute of Comprehensive Utilization of Minerals, Chinese Academy of Geological Sciences, for their assistance with the experimental work.

**Conflicts of Interest:** The authors declare that they have no known competing financial interests or personal relationships that could have influenced the work reported in this paper.

## References

1. Chen, C.; Han, Y.; Zhang, Y.; Liu, Y.; Liu, Y. Efficient Utilization of Siderite- and Hematite-Mixed Ore by Suspension Magnetization Roasting: A Pilot-Scale Study. *Sustainability* **2022**, *14*, 10353. [CrossRef]
2. Messai, A.; Idres, A.; Menéndez-Aguado, J.M. Application of Dry High-Intensity Magnetic Separation in Upgrading Low-Grade Iron Ore of Rouina Deposit, Algeria. *J. Min. Metall. Sect. A Min.* **2020**, *56*, 47–58. [CrossRef]
3. Tang, C.; Guo, Z.; Pan, J.; Zhu, D.; Li, S.; Yang, C.; Tian, H. Current Situation of Carbon Emissions and Countermeasures in China's Ironmaking Industry. *Int. J. Miner. Metall. Mater.* **2023**, *30*, 1633–1650. [CrossRef]
4. Meng, J.; Wang, Q.; Liu, X.; Sun, S.; Li, D.; Zhao, Z.; Yang, Z.; Wu, J. Mineralogy and Geochemistry of the Pangjiazhuang Bauxite Deposit in Jiaokou County, Shanxi Province. *Geol. Explor.* **2011**, *47*, 593–604. (In Chinese)
5. Xue, Y.; Pan, J.; Zhu, D.; Guo, Z.; Yang, C.; Lu, L.; Tian, H. Improving High-Alumina Iron Ores Processing via the Investigation of the Influence of Alumina Concentration and Type on High-Temperature Characteristics. *Minerals* **2020**, *10*, 802. [CrossRef]
6. Alvim, E.S.; Lima, R.M.F. Selective Flocculation/Magnetic Separation of Ultrafine Iron Ore Particles with Corn Starch and Polyacrylamides: A Comparative Study. *Miner. Process. Extr. Metall. Rev.* **2024**, *45*, 606–615. [CrossRef]
7. Bawani, M.R.; Anjum, W.; Almani, S.; Hassan, A.; Raja, R.; Lashari, N.M. Improving the Iron Grade of Indigenous Laterite Ore through Gravity and Magnetic Separation. *Mehran Univ. Res. J. Eng. Technol.* **2025**, *44*, 74–82. [CrossRef]
8. Patra, A.S.; Nulakani, N.V.R.; Kumar, Y.P.; Subramanian, V.; Dash, J.; Mukherjee, A. Design and Synthesis of Novel Polyamine Collector to Recover Iron Values from Iron Ore Slimes. *Powder Technol.* **2018**, *325*, 180–191. [CrossRef]
9. Liu, X.H.; Luo, L.F.; Liu, W.; Chen, W. Research on Beneficiation Process for Low-Grade Limonite Ore. *Min. Metall. Eng.* **2013**, *33*, 70–73. (In Chinese) [CrossRef]
10. Zhang, X.; Zhou, Z.; Gao, P.; Han, Y. Enhanced Iron Extraction from High-Phosphorus Waste Limonite Ore via Suspension Magnetization Roasting: A Pilot-Scale Study. *J. Clean. Prod.* **2023**, *424*, 138860. [CrossRef]
11. Yu, J.; Han, Y.; Li, Y.; Gao, P. Recent Advances in Magnetization Roasting of Refractory Iron Ores: A Technological Review in the Past Decade. *Miner. Process. Extr. Metall. Rev.* **2020**, *41*, 349–359. [CrossRef]
12. Xiao, J.; Ding, W.; Peng, Y.; Wu, Q.; Chen, Z.; Wang, Z.; Wang, J.; Peng, T. Upgrading Iron and Removing Phosphorus of High Phosphorus Oolitic Iron Ore by Segregation Roasting with Calcium Chloride and Calcium Hypochlorite. *J. Min. Metall. Sect. B Metall.* **2019**, *55*, 305–314. [CrossRef]
13. Jiang, Y.; Chen, L.; Duan, S.; Gao, Q.; Yi, F.; Xian, Y. Deep Insight on the Occurrence Feature of Iron Minerals in a Cyanide Leaching Residue and Its Effective Recovery with Magnetic Separation. *Minerals* **2022**, *12*, 524. [CrossRef]
14. Nykänen, V.P.S.; Braga, A.S.; Pinto, T.C.S.; Matai, P.H.L.S.; Lima, N.P.; Leal Filho, L.S.; Monte, M.B.M. True Flotation versus Entrainment in Reverse Cationic Flotation for the Concentration of Iron Ore at Industrial Scale. *Miner. Process. Extr. Metall. Rev.* **2020**, *41*, 11–21. [CrossRef]
15. Silva, K.; Filippov, L.O.; Piçarra, A.; Flilippova, I.V.; Lima, N.; Skliar, A.; Faustino, L.; Filho, L.L. New Perspectives in Iron Ore Flotation: Use of Collector Reagents without Depressants in Reverse Cationic Flotation of Quartz. *Miner. Eng.* **2021**, *170*, 107004. [CrossRef]

16. Swamy, A.K.; Nikkam, S.; Palthur, S.K. Recovery of Hematite from Banded Hematite Quartzite of Southern India by Magnetic Separation and Reverse Flotation. *Minerals* **2022**, *12*, 1095. [CrossRef]
17. Bulayani, M.M.; Raghupatruni, P.; Mamvura, T.; Danha, G. Exploring Low-Grade Iron Ore Beneficiation Techniques: A Comprehensive Review. *Minerals* **2024**, *14*, 796. [CrossRef]
18. Zhang, H.; Zhang, P.; Zhou, F.; Lu, M. Application of Multi-Stage Dynamic Magnetizing Roasting Technology on the Utilization of Cryptocrystalline Oolitic Hematite: A Review. *Int. J. Min. Sci. Technol.* **2022**, *32*, 865–876. [CrossRef]
19. Qiu, Y.; Sun, Y.; Han, Y.; Gao, P. Advanced Strategies for the Efficient Utilization of Refractory Iron Ores via Magnetization Roasting Techniques: A Comprehensive Review. *Miner. Eng.* **2025**, *225*, 109236. [CrossRef]
20. Tang, Z.D.; Gao, P.; Han, Y.X.; Guo, W. Fluidized Bed Roasting Technology in Iron Ores Dressing in China: A Review on Equipment Development and Application Prospect. *J. Min. Metall. Sect. B Metall.* **2019**, *55*, 295–303. [CrossRef]
21. Yuan, S.; Ding, H.; Wang, R.; Zhang, Q.; Li, Y.; Gao, P. The Mechanism of Suspension Reduction on Fe Enrichment with Low-Grade Carbonate-Containing Iron Ore. *Adv. Powder Technol.* **2022**, *33*, 103643. [CrossRef]
22. Li, W.; Chen, J.; Zhou, W.; Han, Y.; Shan, Y. Effect of Bastnaesite as Reductant on Hematite Reduction during In-Situ Suspension Magnetization Roasting of Refractory Iron Ore under Neutral Atmosphere. *Int. J. Min. Sci. Technol.* **2022**, *32*, 877–886. [CrossRef]
23. Zhang, Q.; Sun, Y.; Han, Y.; Li, Y. Pyrolysis Behavior of a Green and Clean Reductant for Suspension Magnetization Roasting. *J. Clean. Prod.* **2020**, *268*, 122173. [CrossRef]
24. Cheng, S.; Han, Y.; Tang, Z.; Li, W. Producing Magnetite Concentrate from Iron Tailings via Suspension Magnetization Roasting: A Pilot-Scale Study. *Sep. Sci. Technol.* **2023**, *58*, 1372–1382. [CrossRef]
25. Jin, J.; Zhu, X.; Li, P.; Li, Y.; Han, Y. Clean Utilization of Limonite Ore by Suspension Magnetization Roasting Technology. *Minerals* **2022**, *12*, 260. [CrossRef]
26. Sun, Y.; Zhu, X.; Han, Y.; Li, Y.; Gao, P. Iron Recovery from Refractory Limonite Ore Using Suspension Magnetization Roasting: A Pilot-Scale Study. *J. Clean. Prod.* **2020**, *261*, 121221. [CrossRef]
27. Monzavi, M.; Raygan, S. Beneficiation of an Oolitic-Iron Ore by Magnetization Roasting and Magnetic Separation. *Iran. J. Mater. Sci. Eng.* **2020**, *17*, 17–29. [CrossRef]
28. Jang, K.O.; Nunna, V.R.M.; Hapugoda, S.; Nguyen, A.V.; Bruckard, W.J. Chemical and Mineral Transformation of a Low Grade Goethite Ore by Dehydroxylation, Reduction Roasting and Magnetic Separation. *Miner. Eng.* **2014**, *60*, 14–22. [CrossRef]
29. Kang, X.; Yu, J.; Sun, H.; Li, Y.; Gao, P.; Han, Y. Growth Behavior and Kinetics of Magnetite during Suspension Magnetization Roasting of Hematite: Coupled Effects of Temperature and CO Concentration. *J. Alloys Compd.* **2025**, *1044*, 184579. [CrossRef]
30. Wills, B.A.; Finch, J.A. *Wills' Mineral Processing Technology: An Introduction to the Practical Aspects of Ore Treatment and Mineral Recovery*, 8th ed.; Butterworth-Heinemann: Oxford, UK, 2016; ISBN 978-0-08-097053-0.
31. *GB/T 6730.5-2022*; Iron Ores—Determination of Total Iron Content—Titrimetric Methods After Titanium(III) Chloride Reduction. Standards Press of China: Beijing, China, 2022.
32. Bale, C.W.; Bélisle, E.; Chartrand, P.; Decterov, S.A.; Eriksson, G.; Gheribi, A.E.; Hack, K.; Jung, I.-H.; Kang, Y.-B.; Melançon, J.; et al. FactSage Thermochemical Software and Databases, 2010–2016. *Calphad* **2016**, *54*, 35–53. [CrossRef]
33. *DZG 20.01-2011*; Rock and Mineral Analysis. Geological Publishing House: Beijing, China, 2011.
34. Nunna, V.; Suthers, S.P.; Pownceby, M.I.; Sparrow, G.J. Beneficiation Strategies for Removal of Silica and Alumina from Low-Grade Hematite–Goethite Iron Ores. *Miner. Process. Extr. Metall. Rev.* **2022**, *43*, 1049–1067. [CrossRef]
35. Zhou, X.; Zhu, D.; Pan, J.; Luo, Y.; Liu, X. Upgrading of High-Aluminium Hematite-Limonite Ore by High Temperature Reduction-Wet Magnetic Separation Process. *Metals* **2016**, *6*, 57. [CrossRef]
36. Basha, S.M.; Biswas, P.; Dwarapudi, S.; Misra, S.; Kamaraj, A. Mineralogical Characterization and Thermal Behavior of High-Alumina Iron Ore Fines. *J. Sustain. Metall.* **2026**, *12*, 2318–2335. [CrossRef]
37. Rath, S.S.; Sahoo, H.; Dhawan, N.; Rao, D.S.; Das, B.; Mishra, B.K. Beneficiation Studies of a Difficult to Treat Iron Ore Using Conventional and Microwave Roasting. *Powder Technol.* **2016**, *301*, 1136–1144. [CrossRef]
38. Yuan, S.; Zhou, W.; Han, Y.; Li, Y. Selective Enrichment of Iron Particles from Complex Refractory Hematite–Goethite Ore by Coal-Based Reduction and Magnetic Separation. *Powder Technol.* **2020**, *367*, 305–316. [CrossRef]
39. Hou, P.; Gao, P.; Yuan, S.; Han, Y.; Sun, Y. Mechanism of Effective Iron Extraction from Rare Earth-Bearing Iron Ores by Low-Temperature Suspension Reduction Method. *Physicochem. Probl. Miner. Process.* **2025**, *61*, 204110. [CrossRef]
40. Zhang, Q.; Sun, Y.; Han, Y.; Li, Y.; Gao, P. Reaction Behavior and Non-Isothermal Kinetics of Suspension Magnetization Roasting of Limonite and Siderite. *Int. J. Miner. Metall. Mater.* **2023**, *30*, 824–833. [CrossRef]
41. Kou, J.; Sun, T.; Tao, D.; Cao, Y.; Xu, C. Coal-Based Direct Reduction and Magnetic Separation of Lump Hematite Ore. *Min. Metall. Explor.* **2014**, *31*, 150–161. [CrossRef]
42. Zhang, W.; Yu, X.B.; Li, L.; Zou, Z.S.; Qi, Y.H.; Xue, Z.L. Effect of Nonstoichiometry on the Thermodynamic Equilibrium of Iron Oxide Reduction Processes. *Chin. J. Eng.* **2015**, *37*, 1291–1295. (In Chinese)
43. Chen, Z.; Chou, K.C.; Morita, K. Mechanism of Metastable Wüstite Formation in the Reduction Process of Iron Oxide below 570 °C. *Mater. Trans.* **2016**, *57*, 1660–1663. [CrossRef]

44. Ansah, E.; Triastomo, R.; Rhamdani, A.R.; Sabah, S.; Brooks, G.A.; Rhamdhani, M.A.; Pownceby, M.I. Thermodynamic Comparison of Fayalite Formation in Low-Grade DRI under CO, CO–H2, and H2-Based Reduction Environments. *J. Sustain. Metall.* **2026**, *12*, 4613–4619. [CrossRef]
45. Rhamdani, A.R.; Sabah, S.; Brooks, G.; Rhamdhani, M.A. Fayalite Formation in the Hydrogen Reduction of Iron Ore and Strategies to Reduce It from a Thermodynamic Perspective. *J. Sustain. Metall.* **2026**, *Epub ahead of printing*. [CrossRef]
46. Wu, S.-C.; Li, Z.-Y.; Sun, T.-C.; Kou, J.; Li, X.-H. Effect of Additives on Iron Recovery and Dephosphorization by Reduction Roasting–Magnetic Separation of Refractory High-Phosphorus Iron Ore. *Int. J. Miner. Metall. Mater.* **2021**, *28*, 1908–1916. [CrossRef]
47. Zhou, X.; Luo, Y.; Chen, T.; Zhu, D. Enhancing the Reduction of High-Aluminum Iron Ore by Synergistic Reducing with High-Manganese Iron Ore. *Metals* **2019**, *9*, 15. [CrossRef]
48. Mendiara, T.; Abad, A.; de Diego, L.F.; García-Labiano, F.; Gayán, P.; Adánez, J. Reduction and Oxidation Kinetics of Tierga Iron Ore for Chemical Looping Combustion with Diverse Fuels. *Chem. Eng. J.* **2019**, *359*, 37–46. [CrossRef]
49. Zhu, C.; Gan, S.; Zhu, Y.; Peng, Z.; Hu, P. A Novel Method for Efficient Recovery of Iron from Hematite: Thermal Storage and Cooling Magnetization Technology, and Alleviating High-Temperature Sintering of Mineral Particles. *Miner. Eng.* **2026**, *247*, 110468. [CrossRef]
50. Nunna, V.; Hapugoda, S.; Pownceby, M.I.; Sparrow, G.J. Beneficiation of Low-Grade, Goethite-Rich Iron Ore Using Microwave-Assisted Magnetizing Roasting. *Miner. Eng.* **2021**, *166*, 106826. [CrossRef]
51. Indian Bureau of Mines. *Monograph on Iron Ore*; Indian Bureau of Mines: Nagpur, India, 2011; pp. 8.8.1–8.8.1.3.
52. Daou, I.; Mocuta, C.; Lecomte-Nana, G.L.; Tessier-Doyen, N.; Peyratout, C.; Guinebretière, R.; Thiaudière, D. Dehydroxylation of Kaolinite and Halloysite-Rich Samples: An In Situ Study of the Texture and Structural Evolutions. *Minerals* **2023**, *13*, 1418. [CrossRef]
53. Saeidfirozeh, H.; Myakalwar, A.K.; Šeborová, P.; Žabka, J.; Abel, B.; Kubelik, P.; Ferus, M. Towards Advanced Mineral Identification for Future Space Mining Applications Employing LIBS and Machine Learning. *J. Anal. At. Spectrom.* **2026**, *41*, 615–632. [CrossRef]


**Disclaimer/Publisher's Note:** The statements, opinions and data contained in all publications are solely those of the individual author(s) and contributor(s) and not of MDPI and/or the editor(s). MDPI and/or the editor(s) disclaim responsibility for any injury to people or property resulting from any ideas, methods, instructions or products referred to in the content.